sLHC Project Note 0041
2012-11-13
Tryfon.Antonakakis@cern.ch

Upgrade of the TCDQ: A dumping protection system for the LHC

Tryfon Antonakakis, Cesare Maglioni / EN-STI

Keywords : LHC, TCDQ, Thermoelasticity, Carbon Fibre Composites, Mobile Diluter

Summary

In the context of the LHC, an asynchronous beam dump could be destructive. In order to ensure the safety of the machine and its surroundings a model of the TCDQ dump has been designed. The length of the TCDQ dump is increased by 50% and its material distribution along its length is changed from graphite to a carbon composite that clearly withstands higher stresses then its counterpart. There are two different density composites used along the dump‘s length in a similar distribution than that of the TCDS, varying from high density to low then back to high. The power deposition within the duration of a pulse is given by FLUKA simulations and is used to predict temperature and stress distributions in space and time. The results are compared with previous studies in which graphite material was used. The difference in the thermal expansion coefficient of the two materials explains the reduced stresses in the newer design.
Due to the high cost of carbon composites an alternative solution is thought without jeopardizing the new design.
The TCDQ diluter design represents one of the main protection elements for the LHC beam dumping system (Weterings, et al., 2012).

1 Introduction to the TCDQ

1.1 Beam characteristics

The TCDQ dump receives an LHC beam of the following characteristics:

- Beam energy: 3.5 -7 TeV
- Beam size: $\sigma_H \, \sigma_V = 0.7 \cdot 0.4 = 0.28 \, mm^2$ ($0.28 \cdot 0.34 = 0.0952 \, mm^2$ for the TCDS beam)
- Number of Bunches: 35
- Bunch to bunch time spacing: 25 ns
- Number of Protons: $1.15 \cdot 10^{11}$ p+/bunch (Nominal LHC) and $2.5 \cdot 10^{11}$ p+/bunch (Ultimate LHC)
- Beam is swept across the cross-section of the dump in the positive x direction (see schematic below).

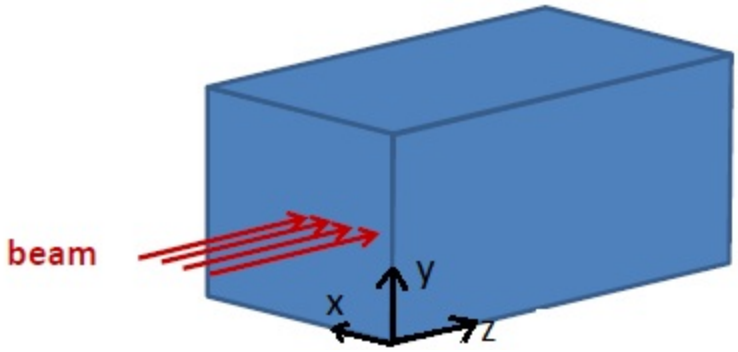

Figure 1: Beam sweeping schematic

A previous study on the TCDS dump has shown some potentially critical situations[1]. Although the beam size and sweep distance is quite different in a positive way (as we will see from the analytical results) there is still need to compute the dynamics of the thermoelastic waves that will emanate from the heat source.

1.2 Bunch locations

Every bunch is injected at a different location on the cross-sectional face of the dump. Let us define the following orientation system as in Figure 1. The origin is at the entrance of the sweep. The (Ox) axis is the sweep axis and the y axis is orthogonal to (Ox) and belongs to the plane orthogonal the sweep plane. Finally the axis (Oz), that we shall refer to as the longitudinal axis is orthogonal to the plane (Oxy).

In the following figures are presented the inter bunch distance spacing for the bunches that intercept the material, i.e. the location of the injection of every bunch on the TCDQ and TCDS. They are uniquely defined by their x coordinate since they are all located on the (Ox) axis.

[1] (Massidda, 2006)

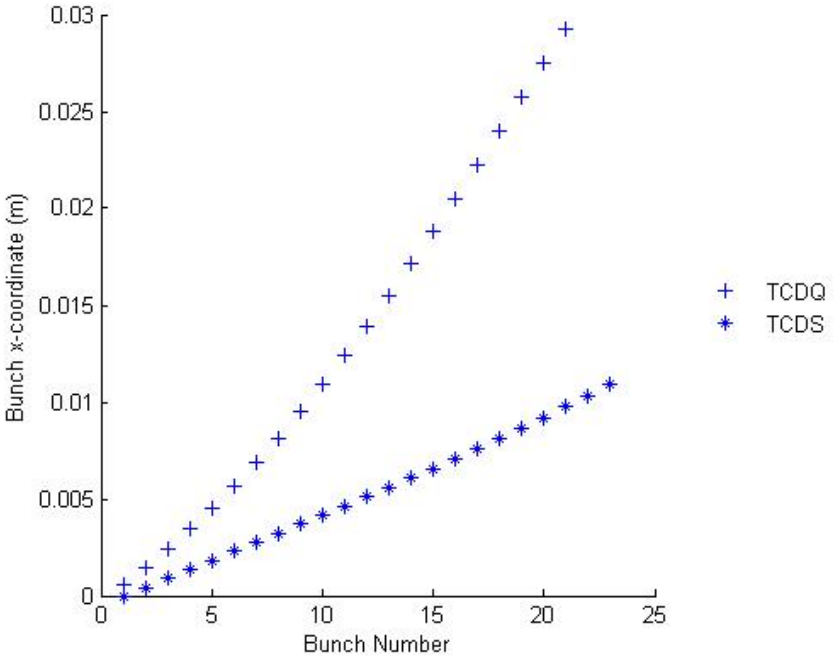

Figure 2: x-coordinate of bunch impact location vs. Bunch number

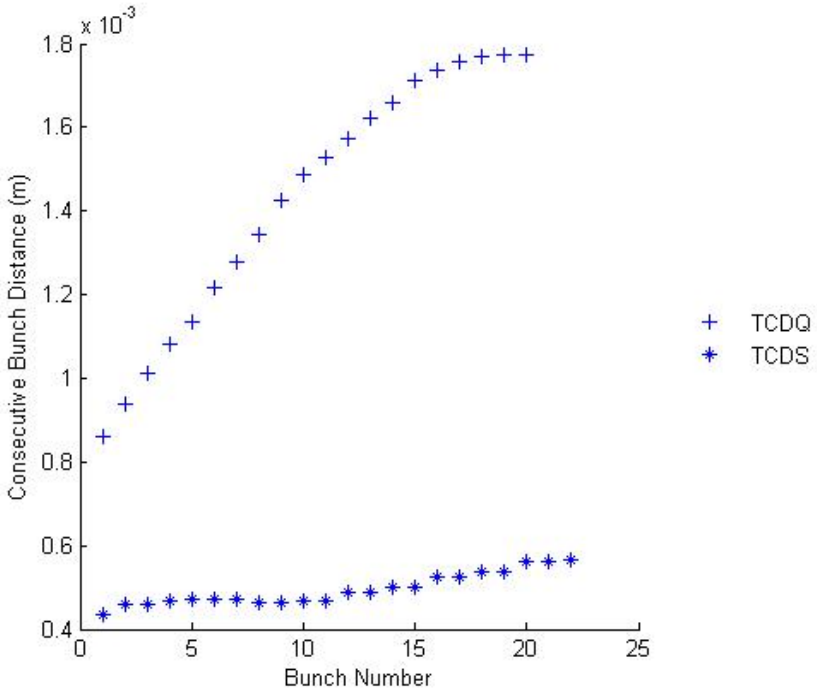

Figure 3: Distance between consecutive bunch impact locations vs. Bunch number

Note the larger spacing for the TCDQ bunches. The combination of different beam sizes and bunch spacings between the TCDQ and the TCDS will have an impact on their respective temperature fields. We assume that only 33 bunches impact the TCDQ so the energy is deposited within $825ns$.

1.3 Material properties discussion and previous TCDQ analysis

Thermally induced stress wave propagation is very sensitive to material parameters[2]. Hence one needs to be very cautious when modelling the properties of a material. Graphite can be modelled as a porous material, hence inserting compacted material properties and porosity ratios, or one could model Graphite as an averaged homogeneous material. It is obvious that the porous material model is more realistic but finding exact compacted graphite properties is tedious[3]. One way is to model compacted properties as Pyrolytic Graphite properties[4] , but that remains very approximate. Modelling porosity matters if the stresses raise enough to result in partial compaction. Simulation results are very sensitive to these choices of material modelling.

In addition to that, one has to choose a Hugoniot shock relation that relates shock wave velocity with material particle velocity[5]. Weak shock relations have an analytical formulation that depends on the Gruneisen coefficient, density and bulk speed of sound[6]. Strong shock relations use experimental constants that yield much stronger stress waves.

Some analytical formulations of the Hugoniot shock relations and the Gruneisen coefficient can be found in[7].

The previous TCDQ design was $6m$ long and its blocks where made of graphite. Previous simulations at nominal LHC intensities combined weak and strong shock Hugoniot relations both within a P-alpha material model, i.e. a porous material model. The results reached Stassi failure limits ($150MPa$) respectively within $12\mu s$ and$1.2\mu s$, for a total time of power deposition of $0.825\mu s$.

The results for the TCDQ were at critical levels and we suggested a change of material and dimensioning of the TCDQ dump, in order to withstand highest LHC beam intensities in the future. The results from the TCDS report[8] were used as a benchmark to change the material, density distribution and length of the TCDQ dump.

1.4 TCDQ: New design

The new length of the beam dump is $9m$. The respective dimensions in each direction $x, y \; and \; z$ depicted in Figure 1 are, $l_x = 45 - 70mm$, $l_y = 70mm$ and $l_z = 250mm$.
The material used is Carbon-Carbon purchased from CVT GmbH & Co. KG.[9], the same material is used in the TCDS dump. CfC is an orthotropic material made of carbon fibres and a graphite matrix. The fibres are in the (Oy) and (Oz) axes.

The following figure shows the density outline of the whole dump.

---

[2] (Davison, 2008)
[3] (Bonnissel M., 2001) (Wen-Shyong Kuo, 2010) (Wang L.W., 2010)
[4] (Coleburn, 1963) (Entwisle, 1962) (Stepovik, 2005)
[5] (Boogerd P., 1995)
[6] (Slater, 1939)
[7] (Brugger K., 1967) (Simons Girard A., 1982) (Boogerd P., 1995) (Doran, 1963)
[8] (Massidda, 2006)
[9] http://www.cv-technology.com/

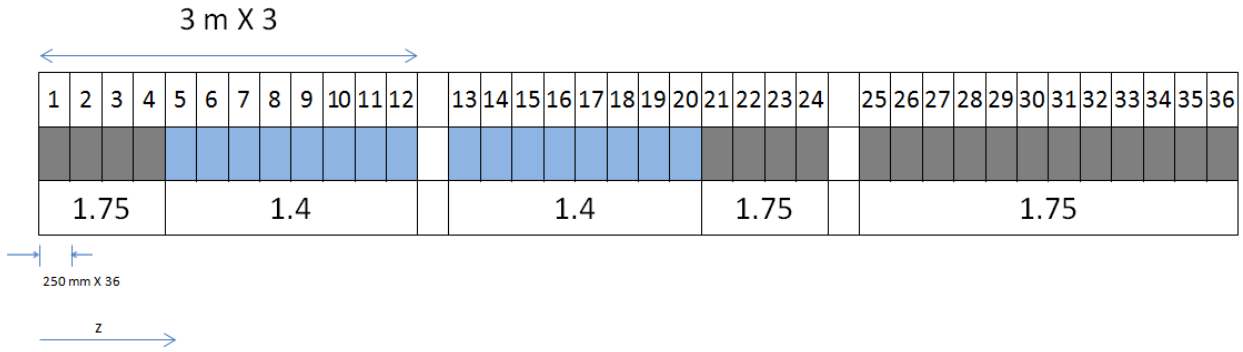

Figure 4: Density outline

The following table provides with a set of material properties used in the simulations[10].

CfC RNFF-SG (at 22 C)		⊥(x)	‖(y)	‖(z)	⊥(x)	‖(y)	‖(z)
Density	g/cm3	1.4			1.75		
Tensile Yield strength	MPa		84	61		84	61
Compresive Yield strength	MPa	69.6	88.6	82.4	69.6	88.6	82.4
Compresive Young Modulus	GPa	2.8	10	10	2.8	10	10
Thermal conductivity	W/mK	91	110	110	91	110	110
3-point bending strength	MPa	170	190	190	170	190	190
3-point bending Young Modulus	GPa	38	40	40	38	40	40

Table 1: Carbon composite material properties

Poisson ratios for each direction are deduced from the respective Poisson ratios of the fibres and the matrix in Appendix A.

Poisson ratio direction	$\nu_{xy} = \nu_{xz}$	$\nu_{zx} = \nu_{yx}$	ν_{yz}
Values	0.0378	0.135	0

Table 2: Poisson ratios for Carbon composites

Specific heat is taken at an average value of $1000\ J \cdot kg^{-1} \cdot K^{-1}$ and the thermal expansion coefficient is taken as the maximum of the three directions as 10^{-6}. Finally to close the orthotropic model we need the shear modulii. Those are not provided by the constructor hence they are determined from similar materials in the literature[11]. The respective in-plane and interlaminar shear modulii are, $G_{yz} = 6.4\ GPa$ and $G_{xy} = G_{xz} = 1.4\ GPa$.

2 Theory

2.1 Notions of thermoelasticity[12]

The underlying equations of thermoelasticity are dependent upon the temperature field as well as the displacement field. Temperature terms appear in the wave equation and displacement

[10] (Massidda, 2006)
[11] (Bradley, et al., 2007)
[12] (Nowacki, 1975)

appears in the diffusion equation. Assuming that the displacement gradients yield a negligible heat source compared to the heat source caused by the beam, one can uncouple the equations of thermoelasticity. The uncoupled thermoelasticity problem reads[13],

$$(\lambda+\mu)\nabla(\nabla\cdot\boldsymbol{u})+\mu\nabla^2\boldsymbol{u}-\alpha(3\lambda+2\mu)\nabla\theta=\rho\frac{\partial^2\boldsymbol{u}}{\partial t^2},$$

$$k\nabla^2\theta=\rho c_v\frac{\partial\theta}{\partial t}-g,$$

where the constants $\lambda,\mu,\rho,\alpha,c_v\ k$ are respectively, the first and second lame parameters in Pa, density in $kg\cdot m^{-3}$, coefficient of thermal expansion in K^{-1}, specific heat in $J\cdot kg^{-1}\cdot K^{-1}$ and coefficient of thermal conductivity in $W\cdot m^{-1}\cdot K^{-1}$. All material parameters are constant in, space and temperature variations. The vector $\boldsymbol{u}$ and the scalar $\theta=T-T_o$ are respectively the displacement field and the temperature difference with respect to the initial temperature T_o assumed to be homogeneous throughout space. Finally g represents a heat source term. Only θ, $\boldsymbol{u}$ and g are dependant on space and time.

2.2 Temperature field

The temperature field solution can be separated in two. In the first time interval the temperature raises rapidly due to the existence of the heat source. In following time interval $g=0$ therefore homogeneous heat diffusion applies. We expect the temperature field at the end of the energy deposition to be similar to the energy deposition field due to the very short time of the power deposition in which heat diffusion is negligible. During the second time interval elastic waves propagate due to the high temperature gradients present while heat diffusion is more apparent.

2.3 Elastic Waves[14]

We now turn to the wave equation that holds the following initial conditions (material is at rest),

$$\boldsymbol{u}_{|t=0}=0\qquad\text{and}\qquad\frac{\partial^2\boldsymbol{u}}{\partial t^2}|_{t=0}=0$$

By taking the divergence and the curl of the equation for displacement we obtain two equations for potentials that yield for the divergence,

$$(\lambda+2\mu)\nabla^2(\nabla\cdot\boldsymbol{u})=\rho\frac{\partial^2\nabla\cdot\boldsymbol{u}}{\partial t^2}+\alpha(3\lambda+2\mu)\nabla^2\theta$$

And for the curl,

$$\mu\nabla^2(\nabla\wedge\boldsymbol{u})=\rho\frac{\partial^2\nabla\wedge\boldsymbol{u}}{\partial t^2}$$

Now set $\boldsymbol{u}=\nabla\phi+\nabla\wedge\boldsymbol{\psi}$ with $\nabla\cdot\boldsymbol{\psi}=0$ then replace in the above equations to obtain the two potential equations, one for the longitudinal wave and the other one for the shear waves.

$$(\lambda+2\mu)\nabla^2\phi=\rho\frac{\partial^2\phi}{\partial t^2}+\alpha(3\lambda+2\mu)\theta$$

$$\mu\nabla^2\boldsymbol{\psi}=\rho\frac{\partial^2\boldsymbol{\psi}}{\partial t^2}$$

[13] (Nowacki, 1975)
[14] (Nowacki, 1975)

Both potential functions have homogeneous initial conditions as a consequence of the initial conditions of $\boldsymbol{u}$. The boundary conditions for $\boldsymbol{u}$ are free surface ones which in turn couples the boundary conditions for the two potentials since $\frac{\partial \boldsymbol{u}}{\partial n} = 0$, where n is the boundary surface normal vector. The temperature acts as a source only for the longitudinal waves as can be seen in the above equation for Φ hence before any reflections we expect to only have longitudinal waves. When the waves reach the boundaries we will have reflected longitudinal waves as well as generation of shear waves that originate from the Neumann type boundary conditions that couple fields Φ and $\boldsymbol{\Psi}$. Nevertheless the main threat lays in the compression waves, hence the need to analyze their source. Let us analyze the different aspects of the source term in the longitudinal wave equation. Before any wave reaches the boundary $\boldsymbol{\psi} = 0$which means that no shear waves are present, so that $\boldsymbol{u} = \nabla\phi$. The link between the temperature difference θ and the strain invariant $\nabla \cdot \boldsymbol{u}$ is linear as predicted from the theory of static thermoelasticity. From the transient term in the displacement equation one can see how the displacement field is dynamically affected. The displacement acceleration is linearly related to the temperature gradients.

3 Simulation setup

Numerical simulations are conducted using AUTODYN software on the block with the highest energy deposition (block 8). Recall that the temperature gradients are responsible for the dynamic behavior of the stresses. For the rest of the blocks we compute numerically the non-diffusive temperature gradients and compare them with block 8. The following results represent the temperature and stress fields for a nominal LHC beam intensity, unless stated otherwise.

3.1 Material model and Equation of State[15]

We chose an orthotropic material model since the carbon-carbon composite chosen for the new TCDQ design is orthotropic. The equation of state's parameters is calculated in the following way:

- Gruneisen Coefficient: $\Gamma = \frac{\alpha_v K}{\rho c_v}$
- C_1 and S_1coefficients in the linear shock Hugoniot relation: $U_s = S_1 u_p + C_1$, where $S_1 = 0.5(1 + \Gamma)$, $C_1 = \sqrt{\frac{K}{\rho}}$, u_p is the particle velocity (in the context of the material's composition) and U_s is the shock velocity.
- Specific heat
- Thermal conductivity

Where α_v, K, ρ, c_v are respectively the volumetric thermal expansion coefficient, Bulk modulus of elasticity, density and specific heat of the material.

Note that there is no orthotropic option for the equation of state so that geometric averaging of the properties in (Table 1: Carbon composite material properties) is used to calculated the necessary parameters used in the above coefficients. Principal stresses are used to identify failure.

[15] (Boogerd P., 1995) (Brugger K., 1967)

3.2 Mesh, time step and CFL condition

Peak temperatures at the end of the pulselength are used to identify each given mesh. Starting from a coarse mesh where the elements are of the order of $2.5mm$, peak temperature rises as we refine the mesh. The peak temperature asymptotic limit is near the non-diffusive temperature. When the peak temperature between two consecutive mesh trials does not rise by more than the desired precision the mesh does not need any further refinement. The final mesh element size in the directions (Ox) and (Oy) is of the order of $1.3mm$. Note that the smaller element size plays a major role in the wave length spectrum that needs to be captured and sets an upper bound for the time step as a consequence of the CFL condition[16]. Assuming that the medium is non-dispersive, and since the element size is chosen to be $1.3mm$ so that the smallest wavelengths captured are of the order of the element size, the highest frequency captured is of the order of 10^6 *Hz.* AUTODYN applies automatically the CFL condition with respect to the smallest element of the model. The frequency cut for a simulation of $100\mu s$ is at $10^7 Hz$ and for a simulation of a single pulselength ($825ns$) is at $10^8 Hz$. Wavelengths of the order of the mesh's elements reflect frequencies of the order of $10^6 Hz$ which will not be cutoff in result of the chosen timestep.

4 Results

4.1 Higher peak energy deposition: Block 8

The peak of energy deposited in the whole TCDQ is found to be in the 8th block[17]. The maximum temperature rise is approximately $\sim 454\ K$ where the non-diffusive temperature rise would be $\sim 461\ K$. The following figure shows the temperature field at the end of the energy deposition.

[16] (Laurence, et al., 1998)
[17] (Versaci, 2012)

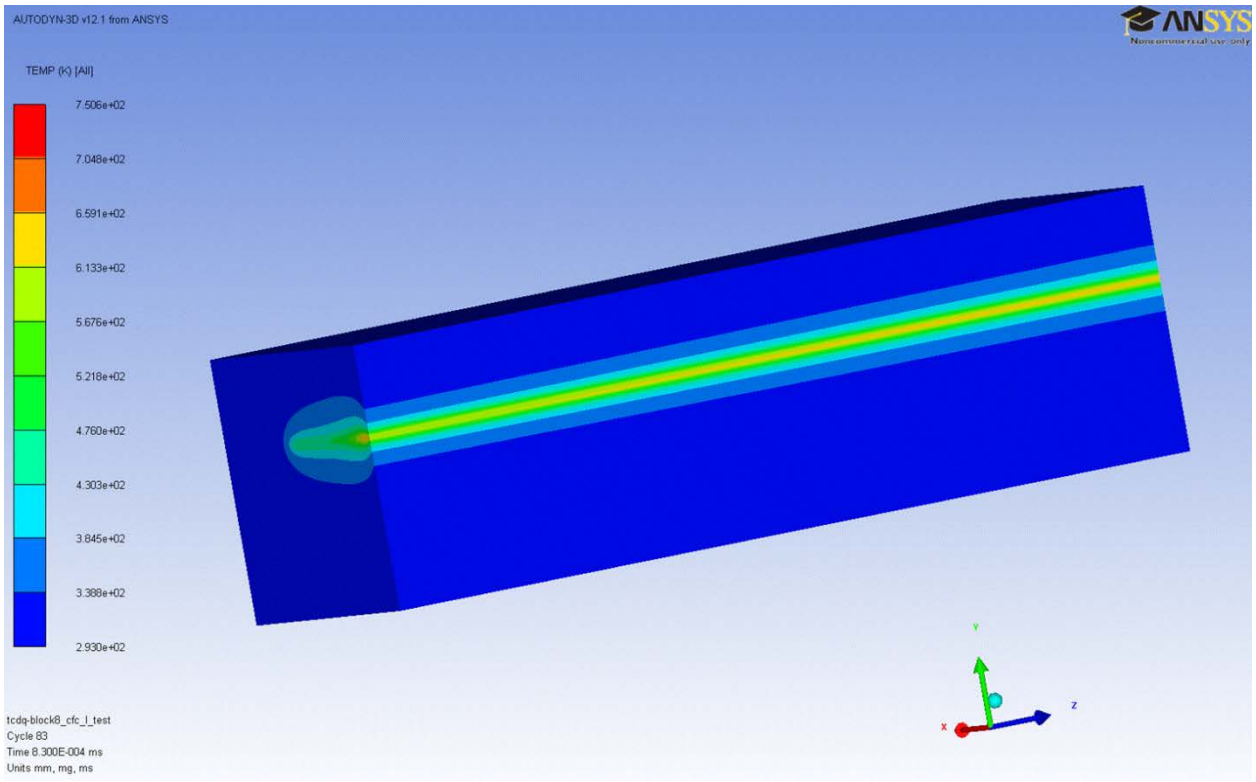

Figure 5: Temperature field

The maximum temperature is reached just a few millimeters inside the block. Figure 6 shows plots for the temperature on a pathline going from point $A(65,0,1805)$ to point $B(65,0,2049)$, coordinates being in mm, for various times during the energy deposition. This pathline is perpendicular to (Oz) and passes near the beam point on plane (Oxy).

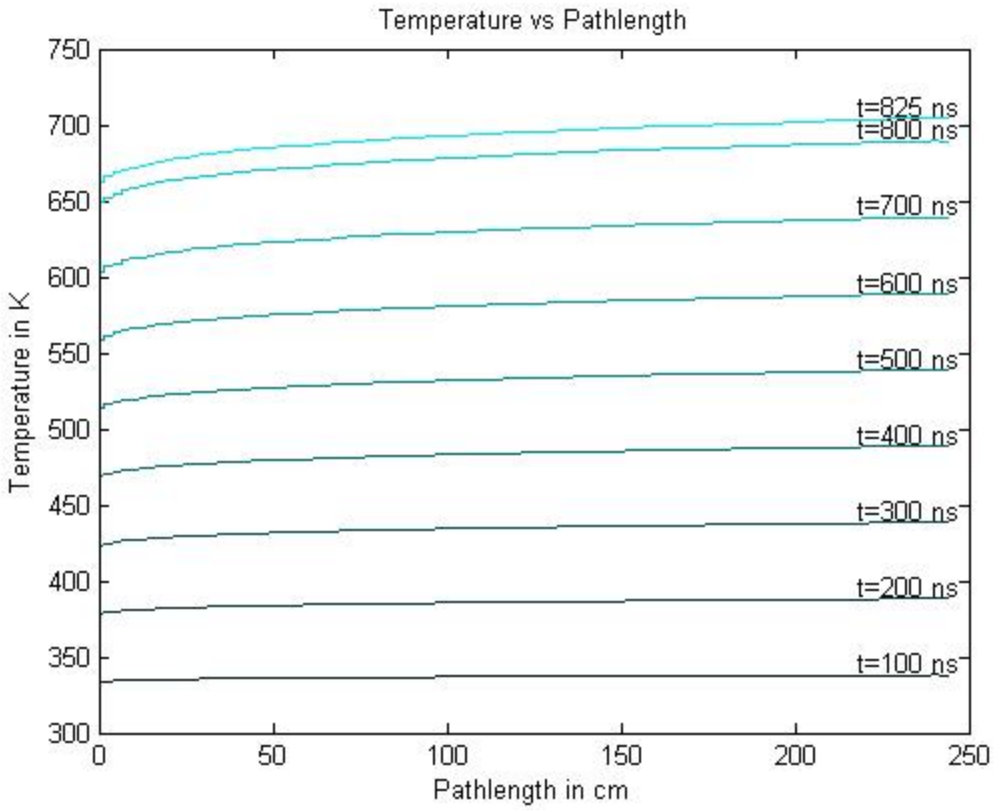

Figure 6: Temperature vs. Pathlength for various times during the energy deposition

The peak temperature is much below the fusion temperature of CfC materials (of the order of $2000K$) so that their crystal properties remain invariant. Let us now turn to the dynamic aspect of this study.

4.2 Stress waves for the homogeneous CfC block

Tensile and compressive YY principal stresses were well below the yield limits ($\sim 80\ MPa$) with respective values of $13.94\ MPa$ and $5.62\ MPa$. The highest tensile stress state happens at a time of $19.5\mu s$ and the highest compressive stress state at a time of $875ns$ i.e. right after the end of the pulse. The following two figures illustrate respectively these tensile and compressive stress states.

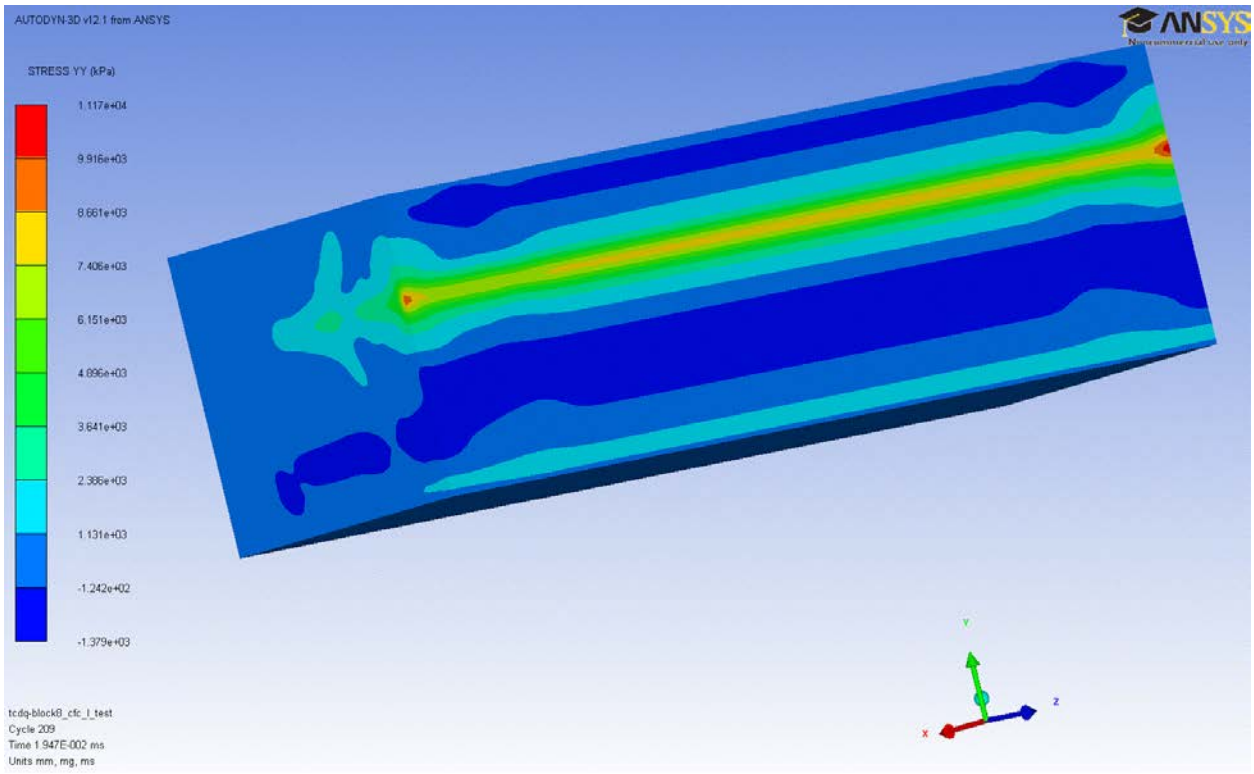

Figure 7: Tensile principal stress YY

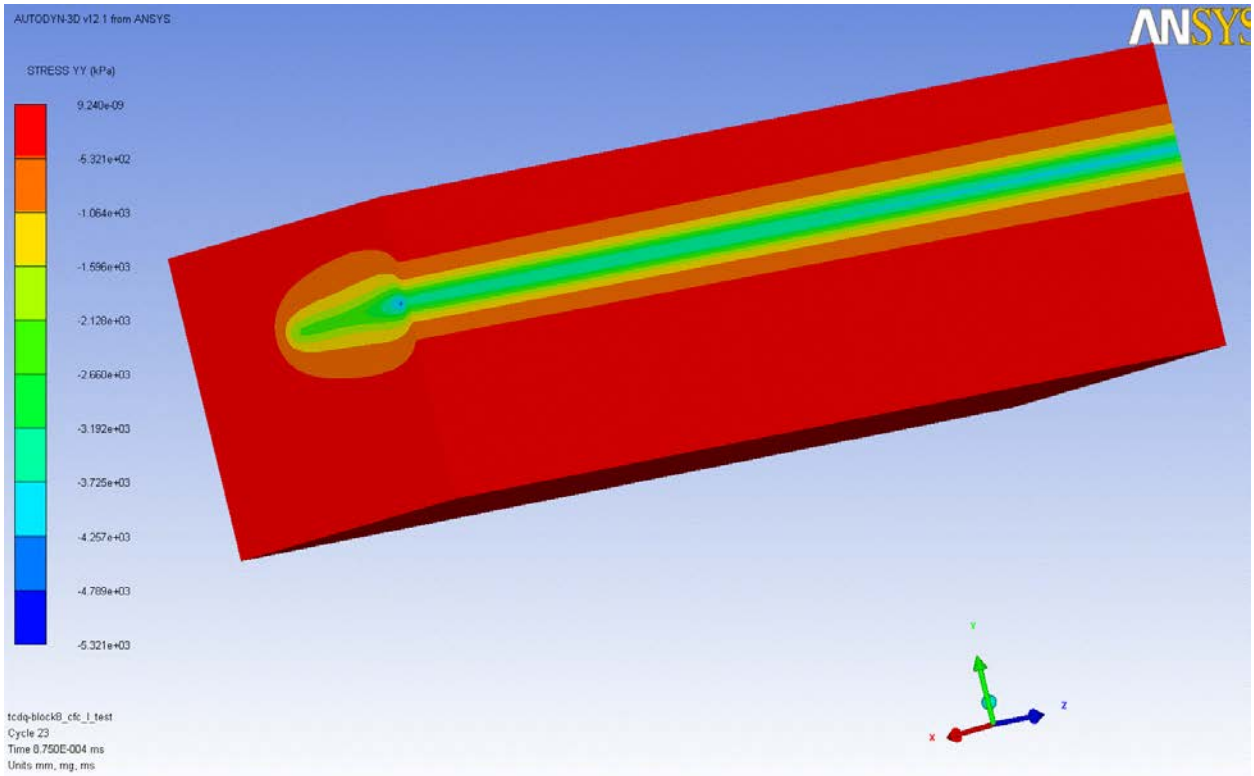

Figure 8: Compressive principal stress YY

The following figures show the time history of principal stresses in the yy direction at different locations in space and these values stay at desired levels.

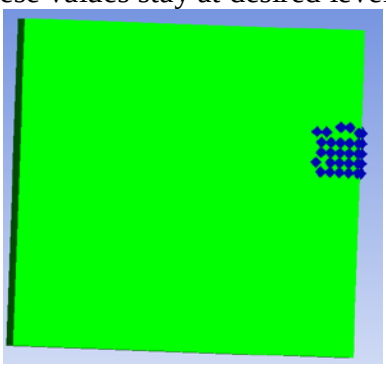

Figure 9: Position of gauge point

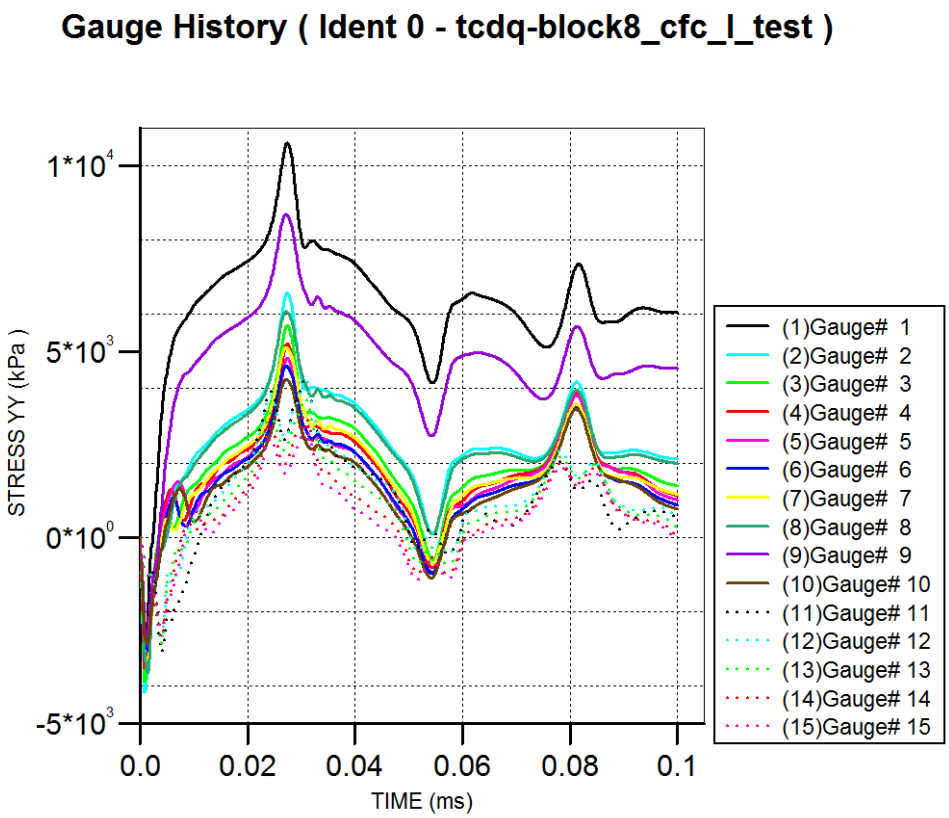

Figure 10: YY principal stresses at various locations in space Vs. Time

4.3 Stress waves for the two material (CfC & graphite) block

Due to high price differences between the CfC and the graphite, it was suggested if a two material block could be used. The homogeneous CfC block is cut at the plane of $x = 40mm$, and the space from $x = 40mm$ to $x = 75mm$ is filled with the previous graphite material. The thermal shock occurring on the graphite part is negligible hence we are only interested in the reflection/refraction, of the stress wave emerging from the beam location, on the material interface. The condition between the two is assumed as bonded so that there should be continuity in all displacements at the material interface. The stress wave propagation direction is

mostly (Oy) parallel to the material interface which yields similar stress fields in the CfC part as in the homogeneous model. Stresses arising in the graphite part are under $3MPa$ in compression which is negligible with respect to the graphite's limit of 125MPa.

4.4 Stress waves for a CfC block shortened in the (Ox) direction

In paragraph 5.3 the boundary conditions at the interface are considered to be of bounded nature. It implies that the waves refracted from the CfC part into the graphite part are of maximum amplitude compared with a more realistic condition where the bond is somewhat loose and more reflection back into the CfC part is expected. Hence the need to test for the other extreme where all waves would be reflected at the material interface back into the CfC part. For that reason a simulation is conducted using only the CfC part with its shortened (Ox) dimension of $40mm$. The stresses do not rise more than in the full (Ox) dimension block. In reality waves propagating in the (Ox) direction will tend to be damped out by a greater amount in the full width block, nonetheless all simulations conducted herein assume a perfectly elastic material with no energy losses which represents the highest possible stress state.

4.5 Non-diffusive temperature gradients for all blocks

The Fluka energy deposition data is directly imported into MATLAB and directly converted to non-diffusive temperature data by the relation, $E = \rho c_v \Delta T$, where E, ρ, c_v and ΔT are in SI units and respectively represent the energy deposited, density, specific heat and temperature rise. A central finite difference scheme is used to compute the spatial temperature gradients at the end of the pulselength.

The maximum temperature gradient out of each block is recorded and each is compared with block 8. Maximum temperature gradients out of all blocks are recorded in block 4, but the ratio of the maximum gradient of block 4 to the one of block 8 is just above 1.08 which cannot increase dynamic stresses significantly with respect to block 8, and definitely not above the material's limits.

4.6 Stress waves for ultimate LCH beam intensity

In the case of an LHC beam intensity of $2.5 \cdot 10^{11}$ p+/bunch (Ultimate LHC) the temperature and stress fields are expected to be more threatening. The maximum temperature rise is of $\sim 994\ K$ and is still below the temperature limits of the material[18]. Highest compression and tensile stress states reach respectively $\sim 10\ MPa$ at the end of the pulselength, and $\sim 24 MPa$ after approximately $20 \mu s$. Both stress states remain under the material limits stated in paragraph 2.3.

[18] (Manocha, 2003)

5 Conclusions

In the case of a nominal intensity beam intercepted by the TCDQ dump, the maximum temperatures reached within the new TCDQ are much below the material's limits. For an ultimate intensity beam temperatures rise to $\sim 1270\ K$ which is still an acceptable value. CfC being an orthotropic material we chose to analyze the resulting stresses from the thermal shock in each of the principle directions. For the ultimate beam intensity stresses reached their highest values in the vertical direction (Oy), and remain below $11\ MPa$ and $25\ MPa$ respectively for the compressive and tensile states. These values are lower than the limits stated in Table 1.

For nominal beam intensity more cost effective design was proposed. It consists of splitting the CfC block in two at the plane of $x = 40mm$ and replacing the CfC material from $x = 40mm$ to $x = 75mm$ with the previous graphite material. This design introduces an interface at the cutting plane which needs to be taken into account. Computations representing worst case scenarios for the CfC and the graphite part were conducted and the results remained similar to the ones where a homogeneous CfC material part was considered.

A. Appendix

Let ν_f and ν_m be respectively the fiber and matrix Poisson ratio – the matrix being graphite, an isotropic material. Also let V_f and V_m be the respective phase volume fractions. The composite material density is:

$$\rho_c = \rho_m \cdot V_m + \rho_f V_f$$

Then we can obtain the directional Poisson ratios by the following formula given in tensor notation,

$$\nu_{ij} = \nu_{f_{ij}} \cdot V_f + \nu_m \cdot V_m$$

The fibre mesh is position in the (Oyz) plane. Let the major Poisson ration of the fibre be $\nu_{f_{yi}} = \nu_{f_{zi}} = 0.2$ where i index can designate any of the three coordinate directions. This only means that the only non zero Poisson ration for a fibre is obtained by applying a force along the fibre's direction and noticing a contraction of its radius. It is assumed that applying radial stress on the fibre does not provoke and longitudinal strain so that, $\nu_{f_{xy}} = \nu_{f_{xz}} = 0$.

In the composites used the following volumetric ratios have been given by the provider, $V_f = 0.3$, hence $V_m = 0.7$. Using the above formulation and the isotropic Poisson ratio for the graphite matrix, $\nu_m = 0.15$ we can compute the composite's Poisson ratios in all directions. They are presented in the following table. First we calculate $\nu_{zx} = \nu_{yx}$ then we can deduce ν_{xy} and ν_{xz} from the symmetry of the strain tensor in the following way[19],

$$\frac{\nu_{xy}}{E_x} = \frac{\nu_{yx}}{E_y}, \frac{\nu_{xz}}{E_x} = \frac{\nu_{zx}}{E_z} \text{ and } \frac{\nu_{yz}}{E_y} = \frac{\nu_{zy}}{E_z}$$

Finally for $\nu_{yz} = \nu_{zy} = 0$ since any deformation in either y or z directions will only yield a resultant deformation in x (since the other direction is reinforced). Note that when we calculate the Poisson ratios for each ν_{zx}, ν_{yx} we only take a volumetric ratio of 0.15 since we take into account only the fibres along the direction of applied load.

[19] (Boresi, et al., 1993)

Bibliography

Arienti M., M. E. S. J., 2004. *Shock and detonation modeling with the Mie-Gruneisen equation of state,* California: s.n.

Barton, G., 1989. *Elements of Green's Functions and Propagation.* Oxford: Oxford Science Publication.

Bina Craig R., S. P. G., 1997. Bulk sound travel times and implication for mantle composition and outer core heterogeneity. *Geophysical Research Letters,* Volume 24, pp. 499-502.

Bonnissel M., L. L. T. D., 2001. Compacted exfoliated natural graphite as heat conduction medium. *Carbon,* Volume 39, pp. 2151-2161.

Boogerd P., V. H. S. M. v. d. S. A. v. d. P. P. S. J., 1995. General shock wave equation of state for solids. *Journal of Applied Physics,* Volume 78, pp. 5335-5344.

Boresi, A. P., Schmidt, R. J. & Sidebottom, O. M., 1993. *Advanced Mechanics of Material.* New York: John Wiley & Sons, Inc..

Bradley, L. R., Bowen, C. R., McEnaney, B. & Johnson, D. C., 2007. Shear properties of a carbon/carbon composite with non-woven felt and continuous fibre reinforcement layers. *Carbon,* pp. 2178-2187.

Brugger K., F. T., 1967. Gruneisen Gamma from Elastic Data. *Physical Review,* 157(3).

Cho, J., Chen, J. Y. & Daniel, I. M., 2007. Mechanical enhancement of carbon fiber/epoxy composites by graphite nanoplatelet reinforcement. *Scripta Materialia,* pp. 685-688.

Coleburn, N., 1963. Compressibility of Pyrolytic Graphite. *The Journal of Chemical Physics,* Volume 40, pp. 71-77.

Davison, L., 2008. *Fundamentals of Shock Wave Propagation in Solids.* Tijeras: Springer.

Doran, D., 1963. Hugoniot Equation of State of Pyrolytic Graphite to 300 kbars. *Journal of Applied Physics,* 34(4), pp. 844-851.

Entwisle, F., 1962. Thermal Expansion of Pyrolytic Graphite. *Physics Letters,* 2(5), pp. 236-238.

Hereil P.-L., A. O. G. M., 1997. Shock behavior of 3D carboncarbon composite. *Journal de Physique IV,* pp. C3-529/C3-534.

Laurence, L. R., Slawinski, R. & Bording, P. R., 1998. *A recipe for stability of finite-difference wave equation computations,* s.l.: s.n.

Manocha, L. M., 2003. High performance carbon-carbon composites. *Sadhana,* Volume 28, pp. 349-358.

Massidda, L., 2006. *Structural analysis of the TCDS collimator: New design,* Pula: s.n.

Nowacki, W., 1975. *Dynamic problems of thermoelasticity.* Warszawa: PWN-Polish Scientific Publishers.

Simons Girard A., L. H. H., 1982. An analytic model for the shock Hugoniot in porous materials. *Journal of Applied Physics,* 53(2), pp. 943-947.

Slater, J. C., 1939. *Introduction to Chemical Physics.* New York: McGraw-Hill.

Stepovik, A., 2005. Measurement of the Gruneisen coefficient of some anisotropic carbon materials. *Journal of Applied Mechanics and Technical Physics,* Volume 46, pp. 911-917.

Versaci, R., 2012. *Evaluation of the energy deposition in the event of an asynchronous beam dump for a 7TeV beam on the new TCDQ model proposed for the LHC,* Geneva: CERN.

Wang L.W., T.-T. Z. M. S. C. R. W. R., 2010. Anisotropic thermal conductivity and permeability of compacted expanded natural graphite. *Applied Thermal Engineering,* Volume 30, pp. 1805-1811.

Wen-Shyong Kuo, T.-H. K. H.-F. L., 2010. On the thermally conductive behavior of compacted graphite nanosheets. *Micro & Nano Letters,* Volume 5, pp. 219-221.
Weterings, W. et al., 2012. *Upgrade of the LHC beam dumping protection elements.* New Orleans, IPAC 12.